Geoderma 459 (2025) 117376

Contents lists available at ScienceDirect

Geoderma

journal homepage: www.elsevier.com/locate/geoderma

Characterization of imogolite-type nanoparticles in Podzols: morphology and association with iron

Tove Florén[a,*], Manuel Bartolomé Díaz[b], Geert Cornelis[a], Stephen Hillier[a,c], Jon Petter Gustafsson[a]

[a] Department of Soil and Environment, Swedish University of Agricultural Sciences, P.O Box 7014, SE-75007 Uppsala, Sweden
[b] Department of Analytical Chemistry and Food Technology, Faculty of Chemical Science and Technology, University of Castilla-La Mancha, 1307 Ciudad Real, Spain
[c] The James Hutton Institute, Craigiebuckler, Aberdeen AB15 8QH, United Kingdom

ARTICLE INFO

Handling Editor: Dr Alberto Agnelli

Keywords:
Imogolite-type nanoparticles
Proto-imogolite
Single-particle ICP-MS
TEM
EDS
Podzols

ABSTRACT

Imogolite-type nanoparticles (ITN) are among the most extensively studied particles present in the Bs horizons of Podzols, as they are strongly associated with the adsorption processes of different anions in soils, including phosphate. The aim of this study was to assess the properties of ITN in soil, in order to increase the current knowledge of ITN regarding adsorption models. ITN were isolated from the B horizons of three Swedish Podzols and characterised in terms of size distribution, morphology, elemental composition, and association with iron. Appreciable amounts of ITN were found in two of the three soil samples studied, reaching up to 14 % ITN by mass if all oxalate-extractable Si is assigned to ITN. Furthermore, substantial amounts of Fe were also present in the selected soil samples. Proto-imogolite (PIM) was the predominant form of ITN, suggesting that tubular imogolite have a lower contribution for ion adsorption reactions in Podzols. Three types of PIM morphology were identified: structureless amorphous clusters, fragmented nanotubes, and globular aggregates. The studied PIM, which exhibited a particle size around 50 nm, contained up to 19 % Fe, while no detectable amounts of Fe were found in tubular imogolite. Regarding PIM, Fe atoms were evenly distributed in the structure, providing evidence for the presence of a substituted and/or surface-adsorbed Fe phase, rather than large ferrihydrite clusters. The present study provides novel insights into the properties of ITN and its association with Fe, which will aid in the development of models predicting the fate of oxyanions in Podzols and other ITN-containing soils.

1. Introduction

The fate and transport of several anions in forest soils are strongly impacted by surface complexation reactions on nanosized secondary Al precipitates, which appear in abundance in acidic forest soils in Scandinavia (Gustafsson et al., 1995; Gustafsson, 2006). Imogolite is a paracrystalline secondary Al mineral, while proto-imogolite (PIM) is a noncrystalline precipitate, considered a precursor of imogolite (Levard et al., 2012). Imogolite and proto-imogolite are collectively described using the term imogolite-type nanoparticles (ITN).

The main reason why ITN are of interest is their large specific surface area, which may be as high as 700 to 1500 $m^2\ g^{-1}$ (Parfitt, 2009), although aggregation, for example as a result of drying, can reduce these values considerably (Lenhardt et al., 2021). Moreover, they have a high affinity for a range of environmentally important oxyanions in soil, such as arsenate (AsO_4^{3-}) (Arai et al., 2005), molybdate (MoO_4^{2-}) (Gustafsson and Tiberg, 2015), as well as nutrients such as phosphate (PO_4^{3-}) (Parfitt, 1989), and dissolved organic matter (Lenhardt et al., 2022). Parfitt (2009) studied PO_4^{3-} sorption onto allophane and found that it binds PO_4^{3-} more strongly than ferrihydrite (Fh). In Fennoscandian Podzols, ITN are dominant among the secondary Al precipitates in the B horizon (Gustafsson et al., 1995; Karltun et al., 2000; Mossin et al., 2002). Tuyishime et al. (2022) recently found that a significant part of the soil PO_4^{3-} in Swedish Podzols was adsorbed to secondary Al precipitates, likely ITN.

Even though ITN is likely an important adsorbent for oxyanions in many soils, accurate models are needed to interpret and predict adsorption behaviour in the context of nutrient bioavailability and transport of contaminants among others. Imogolite is composed of a single gibbsite-like sheet bound by unpolymerized Si-tetrahedra, forming hollow nanotubes with average outer and inner diameters of 2.0 and 0.9 nm, respectively (Cradwick et al., 1972). The empirical formula is

---

[*] Corresponding author.
E-mail address: tove.floren@slu.se (T. Florén).

https://doi.org/10.1016/j.geoderma.2025.117376
Received 18 December 2024; Received in revised form 27 May 2025; Accepted 29 May 2025

Table 1
Characteristics of the soil sampling sites.

Study site and horizon	Depth (cm)	Colour	Location	Altitude (masl)	Dominant tree species	Parent material	Soil order
Kloten			59°54′N 15°15′E	327	Norway spruce, Scots pine	Glacial till	Albic Podzol
O	5–0	5YR 1.7/1					
E	0–7	7.5YR 5/2					
Bs1	7–15	5YR 4/6					
Bs2	15–25	5YR 5/8					
Bs3	25–40	10YR 5/6					
BC	40–49	10YR 4/3					
C	49–70	10YR 5/2					
Paskalampa			59°27′N 14°34′E	252	Norway spruce, Scots pine	Glacial till	Albic Podzol
O	6–0	5YR 2/1					
E	0–12	7.5YR 7/1					
Bs1	12–15	5YR 4/6					
Bs2	15–30	5YR 5/8					
Bs3	30–35	10YR 6/8					
C	45–62	10YR 6/4					
Storå			59°43′N 15°09′E	151	Norway spruce, Scots pine	Glacial till	Albic Podzol
O	5–0	2.5YR/2/2					
E	0–12	7.5YR/6/2					
Bs1	12–20	5YR 4/8					
Bs2	20–50	10YR 6/8					
C	50–60	10YR 6/4					

masl: meters above sea level.

$(HO_3)Al_2O_3SiOH$, describing the arrangement of atoms from the outer to the inner wall surface. The outer surface is lined with doubly coordinated $\equiv Al_2OH$ groups, where $\equiv$ is used to denote a surface species. The $\equiv Al_2OH$ groups are largely unreactive although they possess weak structural positive charge. The inner surface consists of $\equiv SiOH$ groups that acquire negative charge, particularly at high pH (Gustafsson, 2001). This local configuration of Si tetrahedra is unique to imogolite and has been referred to as an "imogolite local structure" (ILS) (Levard et al., 2012). At the tube edges, or at defect sites along the tube wall, there are singly coordinated $\equiv AlOH$ groups which are highly reactive and that form strong inner-sphere complexes with several environmentally significant oxyanions over a wide pH range (Arai et al., 2005; Hiemstra and Zhao, 2016; Hiemstra et al., 1999; Wang et al., 2023). PIM is less structurally ordered than imogolite and is typically described as having a roof tile or globular shape, where the gibbsite-like sheet is absent or poorly developed. This leads to a high proportion of singly coordinated $\equiv AlOH$ groups, making PIM far more reactive than tubular imogolite. It is probable that a large part of the ITN in forest soils consist of PIM rather than tubular imogolite, but the relative proportion of PIM and imogolite have not been established. Given that PIM is far more reactive than tubular imogolite, the proportion of PIM vs. imogolite is a central parameter for the reactivity of ITN.

The lack of knowledge regarding the properties of ITN is hindering the development of a mechanistic adsorption framework for ITN. ITN are, in many ways, similar to Fh as they have a large specific surface area, similar surface-charge properties, and an abundance of singly coordinated surface groups able to form strong surface complexes with oxyanions. However, ITN have not been studied as frequently as Fh and their surface properties and role in ion adsorption reactions are less well known. For example, it can be hypothesized that ITN, as already shown for Fh, possess surface-charge properties that depend on nanoparticle size. Hiemstra and Zhao (2016) developed a model for Fh, relating the Stern layer capacitance and surface area to the particle size, and were able to describe PO_4^{3-} and AsO_4^{3-} adsorption of ultra-small Fe-clusters and nuclei, improving our ability to model the importance of Fh for ion adsorption reactions in soil. Similar adsorption models for ITN are absent and, thus, the sorption behaviour of ITN often have to be assumed to be equivalent to that of Fh or gibbsite when predicting the fate and transport of anions in forest soils.

Furthermore, there is a lack of knowledge regarding the nature of the association of ITN with iron, and its effect on the adsorption properties of ITN. Using Mößbauer spectroscopy, Karltun et al. (2000) found evidence for an intergrowth of an Fh-like phase with a magnetically neutral matrix, possibly ITN. An association of ITN or of $Al(OH)_3$-type sorbents with ferric oxides may alter the surface-charge characteristics of both, affecting oxyanion adsorption (Bazilevskaya et al., 2011; Johnston and Chrysochoou, 2016; Karltun et al., 2000; Shafia et al., 2016). Shafia et al. (2015, 2016) found that isomorphic substitution of Al(III) for Fe (III) occurs at octahedral sites, which at high Fe/Al ratios lead to the formation of discrete Fe_2O_3 clusters. The latter formed already at Fe/Al ratios as low as 0.017. While isomorphic substitution as such appears to have a marginal effect on the point of zero charge (PZC) (Shafia et al., 2016), the presence of Fe_2O_3 clusters in the structure will depress the PZC, leading to increased sorption of metal cations such as Cu^{2+} and Cd^{2+} (Arancibia-Miranda et al., 2020). In addition, arsenate adsorption may increase as arsenate forms stronger complexes with Fe than with Al (Tiberg et al., 2020). Studying Pb^{2+} adsorption, Tiberg et al., (2018) found indirect evidence for a higher PZC of the Fh phase in the presence of ITN in a few Spodic Bs horizons.

The objective of this study was to investigate the properties of ITN in forest soils, determining the size, shape and degree of crystallinity of the particles, as well as the nature of the association between ITN and Fe oxides. To this end, high-resolution transmission electron microscopy (HR-TEM) and inductively coupled mass spectrometry in single-particle mode (spICP-MS) were employed to determine the size and shape of ITN on a nanometre scale. Additional techniques such as Fourier transform infrared spectroscopy (FTIR), X-ray powder diffraction (XRPD), and wet chemical extractions were used to provide further insight on the structure, crystallinity, and chemical properties of ITN. The elemental composition of ITN was investigated at a nanometre scale using energy dispersive spectroscopy (EDS), providing novel information on the extent to which substitution of Al for Fe relative adsorption of Fe or colocalisation of ITN with Fe-oxide clusters occur.

2. Materials and methods

2.1. Soil sampling and site characteristics

The B and C horizons from three Podzols were collected from three forested sites in central Sweden (Kloten, Paskalampa, and Storå; Table 1). The three sites are located at 59°N and situated in managed forest. The forest is dominated by Scots pine (*Pinus sylvestris*) and Norway spruce (*Picea abies*) and the field layer by heather (*Calluna vulgaris*), lingonberry (*Vaccinium vitis-ideae*), and blueberry (*Vaccinium myrtillus*). All soils were developed in glacial till and were classified as well drained (Soil Survey Staff, 2022) Albic Podzols (IUSS Working Group, 2022). Subsamples were collected from the upper, middle, and lower Bs horizon by hand using a spade. Munsell soil colours were determined after sampling during daylight in sunny to overcast conditions.

Field moist soils were sieved (<4 mm) and homogenized. Subsamples were air-dried on paper plates for a week in a thermostated room at 30 °C and then sieved again (<2 mm) after drying to remove any remaining coarse material. Field-moist soils were stored in a cold room (+5 °C) in air-tight plastic bags, while air-dried soils were stored at room temperature in plastic bags.

2.2. Preparation of acid-dispersible isolates

Acid-dispersible isolates were obtained by isolating the < 0.5 μm acid-dispersible clay fraction following the method of Farmer et al. (1980). For each sample, 10 g air-dried soil was dispersed in 0.3 mmol L^{-1} HCl (pH 3.5) and then ultrasonicated at high amplitude for 4 min using an ultrasonic probe. Following this protocol, the ITN are dispersed at low pH due to their positive surface charge, whereas other crystalline clay minerals, which otherwise may interfere with the identification of ITN, are not. Although this relatively mild isolation method does not give a complete recovery of ITN, due to the presence of organic matter and to partial dissolution at pH 3.5, it was preferred to other more aggressive isolation methods (e.g. peroxide pre-treatment), which can be expected to significantly alter the morphology of ITN. The samples were centrifuged at 2,900 *g* for 20 min to isolate the ITN-containing supernatant following the method for particle-size fractionation by Jackson (1969). The supernatants were stored in a cold room (+5 °C) until further analysis.

2.3. X-ray powder diffraction (XRPD)

Mineralogical analysis of bulk soil was performed using XRPD. Air-dried and sieved soil samples were micronized in ethanol using a McCrone mill and the resulting slurry was spray-dried (Hillier, 1999). This method produces random powders and minimizes the occurrence of preferred orientation within the sample. The samples were scanned from 4 to 70° 2θ on a Bruker D8 diffractometer with Cu K-α radiation and a Lynxeye XE position sensitive detector. Crystalline minerals were identified using the Bruker DiffracPlus EVA software in conjunction with International Centre for Diffraction Data (ICDD) Powder Diffraction file (PDF-4, 2021). Quantitative mineralogical analysis was carried out using a full pattern fitting approach using the R package powdR, as outlined by Butler and Hillier (2021a). The process involves selecting reference patterns from a pre-prepared library of patterns of pure minerals, the measured XRPD pattern is then fitted by an optimisation process as a weighted sum of reference patterns. By using measured patterns that include background scattering rather than calculated reference patterns which only consider Bragg diffraction, the method allows direct quantification, in weight percent, of both crystalline and amorphous phases. Further details can be found in an example of the application of the method to round robin samples of known composition (Butler and Hillier, 2021b).

2.4. Fourier transform infrared spectroscopy (FTIR)

FTIR was carried out to determine the presence of ITN in acid-dispersible isolates and to characterise crystalline and poorly crystalline metal oxides. The spectra were recorded on a Perkin Elmer Spectrum 100 spectrometer in transmittance mode between 4000 and 400 cm^{-1}. Before analysis, the acid-dispersible isolates were lyophilised and stored in a desiccator to prevent absorption of water from the atmosphere. A 1 mg subsample was pressed together with KBr powder in a hydraulic press and pressed into 13 mm discs and then scanned 16 times.

2.5. Soil pH and chemical extractions

The soil pH was measured using a Radiometer Analytical pH electrode in suspensions of sieved ($<$ 4 mm) field-moist soil and ultrapure MilliQ water (0.055 μS • cm^{-1}) after 24 h of equilibration (soil:water ratio 1:2.5) (van Reeuwijk, 2002). Oxalate-extractable Fe, Al, Si, and P (Fe_{ox}, Al_{ox}, $Si_{ox,}$ and P_{ox}) and pyrophosphate-extractable Al and Fe (Al_{py}, Fe_{py}) were determined by ICP-OES using a Thermo Scientific ICAP 6000 instrument (Thermo Scientific, Waltham, Ma, USA). Oxalate extraction was performed according to the method by McKeague and Day (1966) as used by van Reeuwijk (2002) where 2.00 g sieved ($<$ 2 mm) soil was mixed with 200 mL ammonium oxalate buffer (0.2 mol L^{-1}) at pH 3 and equilibrated in the dark for 4 h in an end-over-end shaker. Pyrophosphate extraction was carried out by mixing 1.00 g of sieved ($<$ 2 mm) soil with 100 mL Na-pyrophosphate solution (0.1 mol L^{-1}) and equilibrated for 16 h in an end-over-end shaker (McKeague, 1967). Pyrophosphate and oxalate extracts were centrifuged for 20 min at 3,800 g and filtered (Aerodisc 0.2 μm syringe filters with Supor membrane) before analysis.

2.6. Single particle ICP-MS analysis

Inductively coupled plasma-mass spectrometry (ICP-MS, Perkin Elmer 350D) was used in single-particle mode to measure the corresponding spherical diameter and number concentration of ITN in acid-dispersible extracts on a particle by particle base. A concentric nebuliser (Element) was used, aspiring solutions at 400 μL min^{-1} in a cyclonic spray chamber (Element). The flow rate was confirmed gravimetrically. The ^{27}Al signal was measured 2×10^6 times both in element standards of known Al concentrations diluted in 0.3 mmol L^{-1} HCl and acid extracts using a measurement of 50 μs without settling time. Similar datasets were obtained both for dissolved Au standards and a 60 nm-size certified Au NIST standard that was diluted 10^7 times allowing to calculate the nebulisation and transfer efficiency based on the method of Pace et al. (2011). All dissolved and particulate Au standards were diluted in 0.1 % cysteine to avoid memory effects or precipitation of neoformed Au nanomaterials (Chen et al., 2000). Instrument control and initial calculations were performed using the Perkin Elmer Syngistix software. Final calculations were performed in a bespoke software (Nanocount). This software uses the deconvolution method (Cornelis and Hassellöv, 2014) to remove the dissolved ^{27}Al signal. Different poly-gaussian models were fitted to signal histograms of dissolved Al standards revealing the blank ^{27}Al signal, sensitivity, flicker noise and shot noise factors. This allowed fitting a poly-gaussian model and the number of exclusively dissolved data points to the frequency of signal magnitudes up to 4 ions of the ^{27}Al signals of unknown samples. The resulting poly-gaussian function was then deconvoluted from the signal histogram of unknown samples leaving a histogram of exclusively particulate signals. Number-based distributions of the corresponding spherical diameter were then calculated assuming all particulate ^{27}Al signals having a stoichiometry of $Al_2SiO_3(OH)_4$ and density of 2.7 g cm^{-3}, based on the properties of imogolite (Wada and Yoshinaga, 1969). Acid-dispersible isolates were measured in four different dilution levels (from dilution $1{:}10^4$ to $1{:}10^7$) to account for the aggregation effect seen at higher concentrations and to avoid the predominance of false positives seen at

Table 2
Selected chemical properties of soil samples.

Horizon	Depth	pH_{H2O}	Al_{ox}	Si_{ox}	Fe_{ox}	P_{ox}	Al_{py}	Fe_{py}	Tot-C	Tot-N	Al_{ox}-Al_{py}:Si_{ox}	Al_{ox}: Fe_{ox}	Al_{ox}:Al_{py}
	(cm)		(mmol kg^{-1})						(%)				
Kloten													
Bs1	7–15	5	1524	392	421	22	465	11	7.1	0.3	2.7	3.6	1060
Bs2	15–25	5.1	669	214	152	8.4	84	14	1.9	0.1	2.7	4.4	586
Bs3	25–40	5.1	334	91	49	4.8	112	21	1.5	0.1	2.5	6.8	223
Paskalampa													
Bs1	12–15	4.2	223	18	233	4.8	162	152	3.6	0.1	3.4	1.0	61
Bs2	15–30	4.9	1580	695	278	4.8	223	33	1.7	0.1	2.0	5.7	1357
Bs3	30–45	5.1	613	342	73	3.2	67	1.8	0.7	0	1.9	8.4	547
C	45–62	5.2	223	89	30	3.2	34	0.9	0.2	0	2.1	7.1	190
Storå													
Bs1	12–20	4.7	262	32	242	3.2	132	51	2.5	0.1	3.9	1.8	126
Bs2	20–50	5.5	475	193	75	6.5	98	11	1.5	0.1	1.9	6.1	586
C	50–60	5.6	160	61	18	3.2	28	2.7	0.4	0	2.2	8.9	223

MC: moisture content, Al_{ox}: oxalate extractable Al, Si_{ox}: oxalate extractable Si, Fe_{ox}: oxalate extractable Fe, P_{ox}: oxalate extractable P, Al_{py}: pyrophosphate extractable Al, Fe_{py}: pyrophosphate extractable Fe, Tot-C: total carbon, Tot-N: total nitrogen, Al_{ox}-Al_{py}: Si_{ox}: ratio of inorganic Al and oxalate extractable Si, Al_{ox}-Al_{py}: inorganic Al.

lower concentrations.

2.7. Transmission electron microscopy (TEM)

Micrographs and spectra were recorded on acid-dispersible isolates. Samples were prepared by placing a drop of acid-dispersible isolate suspension on a Pelco Lacey Formvar/Carbon 300 square copper grid and then set to air-dry before observation. Micrographs were collected on a Titan HR-TEM instrument (FEI) operated at 200 kV. Energy-dispersive spectroscopy (EDS) was used for elemental analysis of the isolates. Spectra and elemental maps were recorded on a Tecnai TEM instrument (FEI) operated at 200 kV with a high-angular dark-field STEM detector. Quantification and image processing was done using the Gatan DigitalMicrograph software (Ametek). The ImageJ software of the National Institute of Health (Rasband, 1997-2018) was used to measure the diameter and length of a discrete number of representative PIM clusters and imogolite nanotubes.

3. Results

3.1. General soil properties and mineralogy

The studied soils were naturally acidic with the pH ranging from 4.2 to 5.6, with the highest pH values in the C horizon (Table 2). In many respects, the soils show similar chemical characteristics as other previously studied Podzols from Sweden (Gustafsson et al., 1999; Karltun et al., 2000; Tuyishime et al., 2022). However, when compared to other Scandinavian Podzols, the Paskalampa and Kloten soils were unusually rich in oxalate-extractable Al (Al_{ox}) and Si (Si_{ox}). The highest contents of Al_{ox} were found in Paskalampa Bs2 and Kloten Bs1 (1580 mmol kg^{-1} and 1524 mmol kg^{-1} respectively). For Paskalampa Bs2 Si_{ox} was as high as 695 mmol kg^{-1}, which corresponds to an ITN content of ~ 14 % of the soil mass, if all Si_{ox} is assigned to ITN. The Fe content varied between soils and horizons but was typically high in the top Bs horizons and then declining with depth. The Fe content was low in comparison to the Al content, as demonstrated by the Al_{ox}:Fe_{ox} ratio.

The mineralogical composition of the bulk soil was determined by X-ray power diffraction (XRPD) (Table S1). The mineralogy of the Kloten soil was previously studied by XRPD by Tuyishime et al. (2022), with very similar results. All three sites were dominated by quartz, plagioclase, and K-feldspar, with amounts that varied very little between the sites and horizons. Beyond that, there were smaller contributions of amphibole, epidote, and garnet, generally below 2 wt%. In agreement with the extraction results, amorphous Al and Fe phases (Am-I) were detected in all samples with especially appreciable mass percentages (> 20 wt%) in Paskalampa Bs2 and Kloten Bs1. Amorphous organic phases were only detected in the upper part of the soil and then at relatively low percentages, except for in Kloten Bs1 where the mass percentage was higher at 7.4 wt%. Amorphous Al and Fe phases were most abundant at upper to intermediate depths.

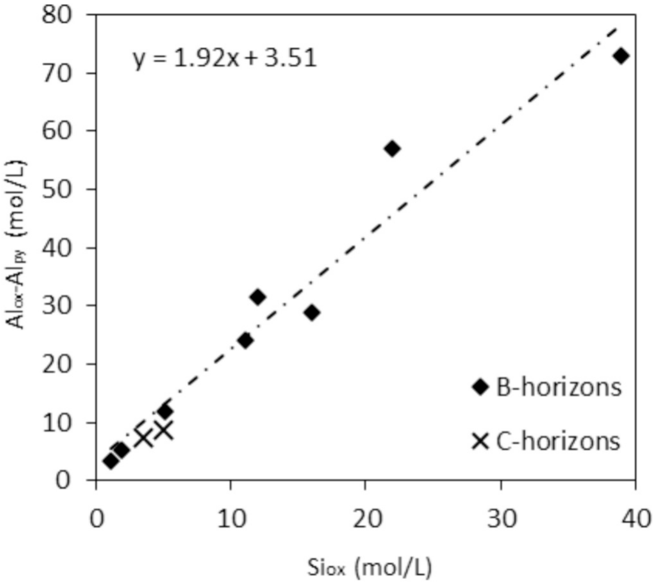

Fig. 1. Relationship between surface reactive inorganic Al_{ox}-Al_{py} and Si_{ox} in the B and C horizons.

The difference between oxalate- and pyrophosphate extractable aluminium (Al_{ox}-Al_{py}) was high in all soils, but particularly high in Paskalampa Bs2 and Kloten Bs1. The inorganic Al:Si ratio was calculated as (Al_{ox}-Al_{py})/ Si_{ox} for each sample, values obtained ranged from 2 to 3 in all cases. The strong linear relationship found between Al_{ox}-Al_{py} and Si_{ox} (Fig. 1) suggests that ITN was the dominant form of surface-reactive inorganic Al in these soils, in line with other studies on Fennoscandian Podzols (Gustafsson et al., 1999, 1995; Lundström et al., 2000).

3.2. Presence and identity of ITN

Fourier transform infrared spectroscopy (FTIR) allows for qualitative assessment of the degree of order, as well as the relative proportions of

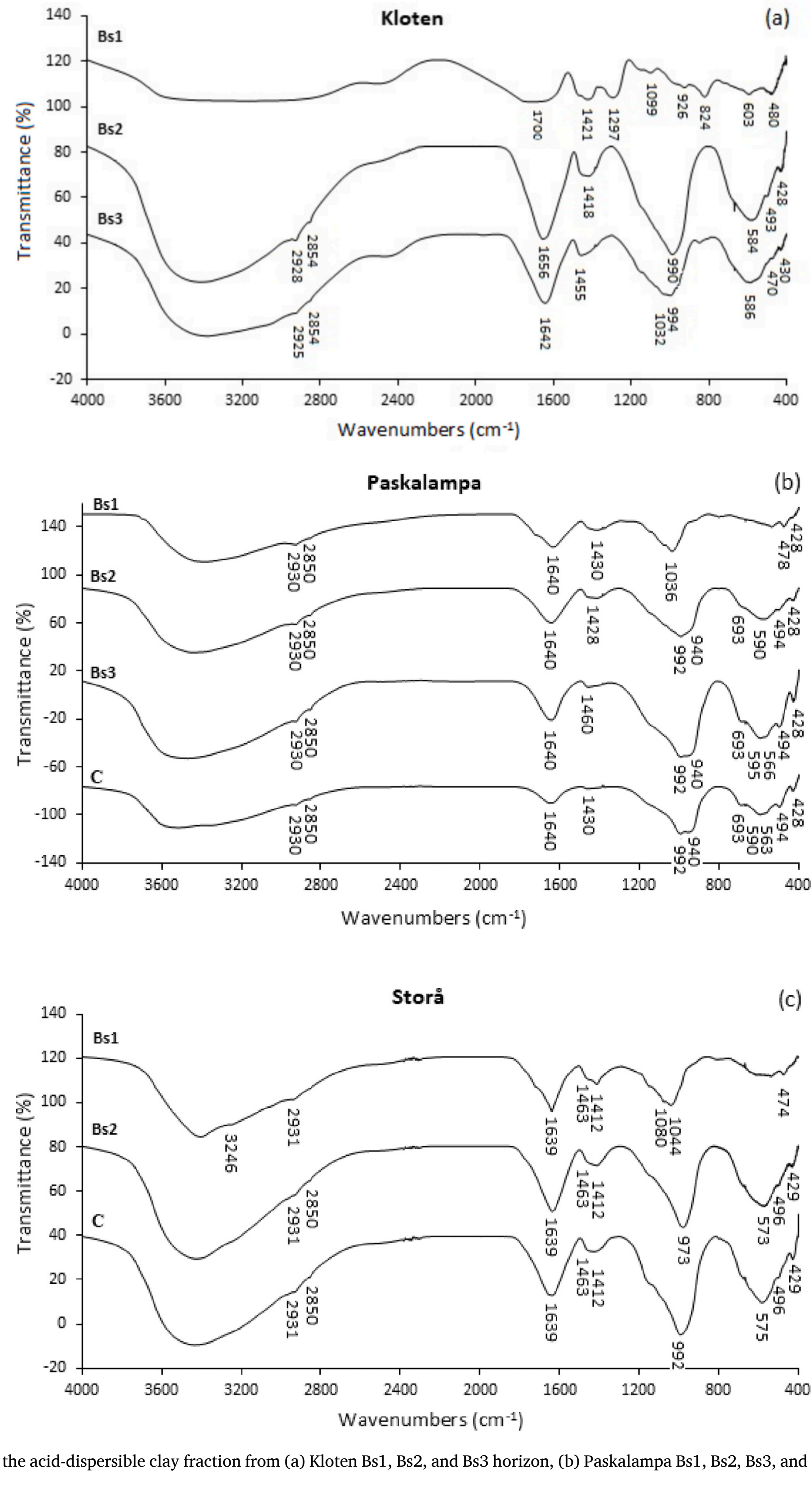

Fig. 2. Infrared spectra of the acid-dispersible clay fraction from (a) Kloten Bs1, Bs2, and Bs3 horizon, (b) Paskalampa Bs1, Bs2, Bs3, and C horizon, and (c) Storå Bs1, Bs2, and C horizon.

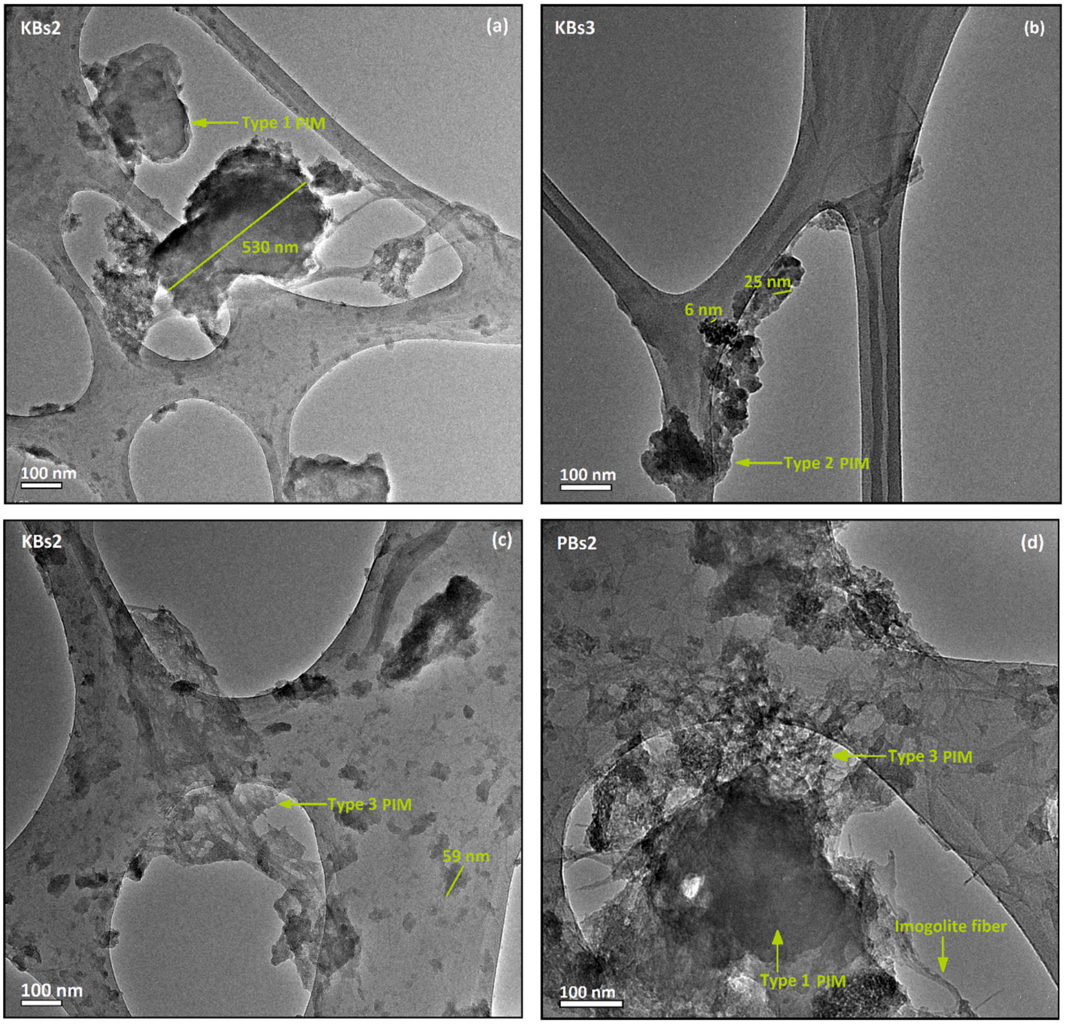

Fig. 3. Micrographs showing PIM clusters with different structural characteristics on lacey carbon films. (a) Type 1 –structureless amorphous compound, (b) type 2 – fragmented nanotubes, (c) type 3 – globular aggregates, and (d) heterogeneous mix of PIM and imogolite.

PIM and imogolite. The most distinct feature of imogolite is a double-peak feature at 992 and 940 cm^{-1} that occurs due to stretching in the orthosilicate structure during curling of the imogolite tube. Another doublet related to ordered imogolite appears at 566 and 595 cm^{-1}. These two double peaks will only be visible when tubular imogolite is present in the sample. Other characteristic absorption bands appear at 693, 494, and 428 cm^{-1} (Arancibia-Miranda et al., 2011; Gustafsson et al., 1995; Parfitt and Hemni, 1980).

The characteristic doublet around 992 and 940 cm^{-1} appeared in the Bs2, Bs3, and C horizon samples of Paskalampa (Fig. 2), indicating that the relative proportion of tubular imogolite increased with increasing depth in the B horizon. No evidence of ITN was observed in the Bs1 horizons, which can be explained by the presence of organic matter that stabilises ITN and prevents it from dispersing. The ITN in Kloten was dominated by PIM, as evidenced by the single broad absorption band at 990 cm^{-1}, together with a set of other characteristic bands in the 400–600 cm^{-1} region. The doublet at 994 and 1032 cm^{-1} in the Bs3 horizon is probably due to a mix of ITN and layer silicates.

The Paskalampa soil had a higher relative proportion of tubular imogolite when compared to Storå and Kloten. The doublet feature at 992 and 940 cm^{-1} appeared in all horizons except Bs1. Further, a doublet feature around 560 and 590 cm^{-1}, also characteristic for tubular imogolite, appeared in the Bs3 and C horizons. The Storå soil showed less distinct ITN features, although diffuse PIM bands were identified in the Bs2 and C horizon.

3.3. *Morphology of ITN*

The acid-dispersible clay fractions of PBs2, PBs3, KBs2, and KBs3 were studied using HR-TEM at different scales. Micrographs confirmed that ITN were plentiful in the acid-dispersible clay fraction, as evidenced by FTIR and selective extractions. The ITN in the Bs2 samples consist of a polydisperse mix of PIM (Fig. 3) and imogolite (Fig. 4). In the extracted ITN, three types of PIM morphology were identified: Type 1 – a structureless amorphous cluster (Fig. 3b), Type 2 – fragmented nanotubes (Fig. 3a), Type 3 – globular aggregates (Fig. 3c). The PIM clusters were often heterogeneous, comprising a mix of PIM intergrown with imogolite (Fig. 3d). Additional images of PIM clusters and imogolite nanotubes are available in the Supplementary materials (Fig. S2).

Tubular imogolite was identified in both Paskalampa and in the Kloten Bs2 and Bs3 samples (Fig. 4). Well-formed nanotubes had a strong tendency to aggregate and to form fibre-like structures between 4 and 50 nm in width. Probably, these structures consisted of bundles or networks of a few up to hundreds of individual imogolite tubes. Short fibres assembled into large agglomerates, often together with PIM (Fig. 4b). Tubular imogolite appeared to some degree in all samples, but the relative proportion clearly increased with depth. Extensive fibrous networks of tubular imogolite were only found in the lower Bs horizons of the Paskalampa soil (Bs2 and Bs3). In these samples, the networks occurred in abundance and grew several micrometres large (Fig. 4c, d).

The median particle diameter (Table 3) and particle-size distribution

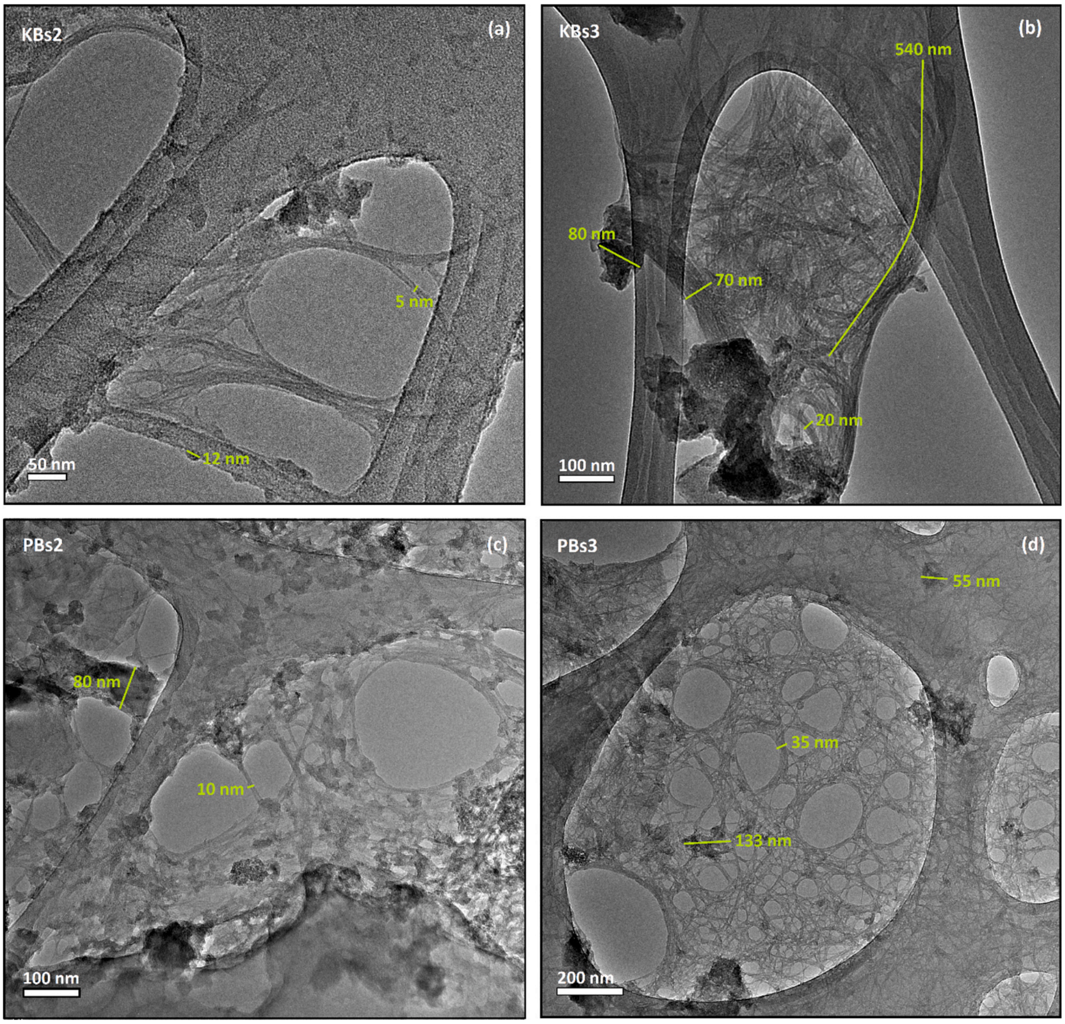

Fig. 4. Micrographs of tubular imogolite extracted from the Bs2 and Bs3 horizons of Paskalampa and Kloten Podzols on lacey carbon films.

Table 3
Particle size of ITN as given by spICP-MS.

Median particle size (nm) for each site and horizon.					
Kloten		Paskalampa		Storå	
Bs1	56	Bs1	53	Bs1	54
Bs2	55	Bs2	52	Bs2	52
Bs3	55	Bs3	54	C	57
		C	57		

(Fig. 5) was determined by spICP-MS. Most particles ranged from 40 to 80 nm in size, which is significantly larger than the known particle size of imogolite. However, it agrees with the observations from HR-TEM, according to which clusters of varying sizes were observed, many of them around 50 nm in size. Thus, it is unlikely that spICP-MS quantified singular particles. More likely, the results are valid for clusters of PIM.

Thus, it appears that the use of spICP-MS only allowed for the size determination of PIM clusters, while ITN fibrous networks and very small PIM clusters may not have been included in the spICP-MS determination. During data treatment, nominally dissolved Al signals were removed during the deconvolution step, which might also remove very small ITN units. However, the observed size range is clearly larger than the expected lowest detectable size of spICP-MS after deconvolution (Cornelis and Hassellöv, 2014). Moreover, the close correspondence between HR-TEM and spICP-MS suggests that the size of the PIM clusters, which probably contain a large part of the most reactive ITN, was correctly captured.

3.4. *Elemental composition of ITN by TEM-EDS*

Elemental mapping of PBs2 and PBs3 (Fig. 6) showed the atomic distribution of Al, Si, and Fe of the acid-dispersible isolates. Al and Si were evenly distributed within the fibrous ITN networks (Fig. 6). Elemental quantification based on the TEM-EDS elemental maps (Table S3) showed that Al and Si were the dominant elements at the sites with around 60 mol % Al and 24 % Si, respectively. Iron did occur (9 and 19 % for PBs2 and PBs3, respectively), but was concentrated to Type 1 PIM only. These Fe contents are high enough to exclude isomorphic substitution of Al for Fe as the only explanation (Shafia et al., 2015). Furthermore, we found no evidence of Fe associated with tubular imogolite. A closer look at a Type 1 PIM cluster (Fig. S3) revealed that the Fe was evenly distributed within the cluster.

4. Discussion

4.1. *Identification and characterisation of ITN*

FTIR and HR-TEM imaging confirmed the abundance of imogolite in the lower part of the Bs horizons where long well-developed nanotubes had arranged themselves into complex networks of thick fibres. Despite the abundance of imogolite, PIM clusters were found amidst the tubular

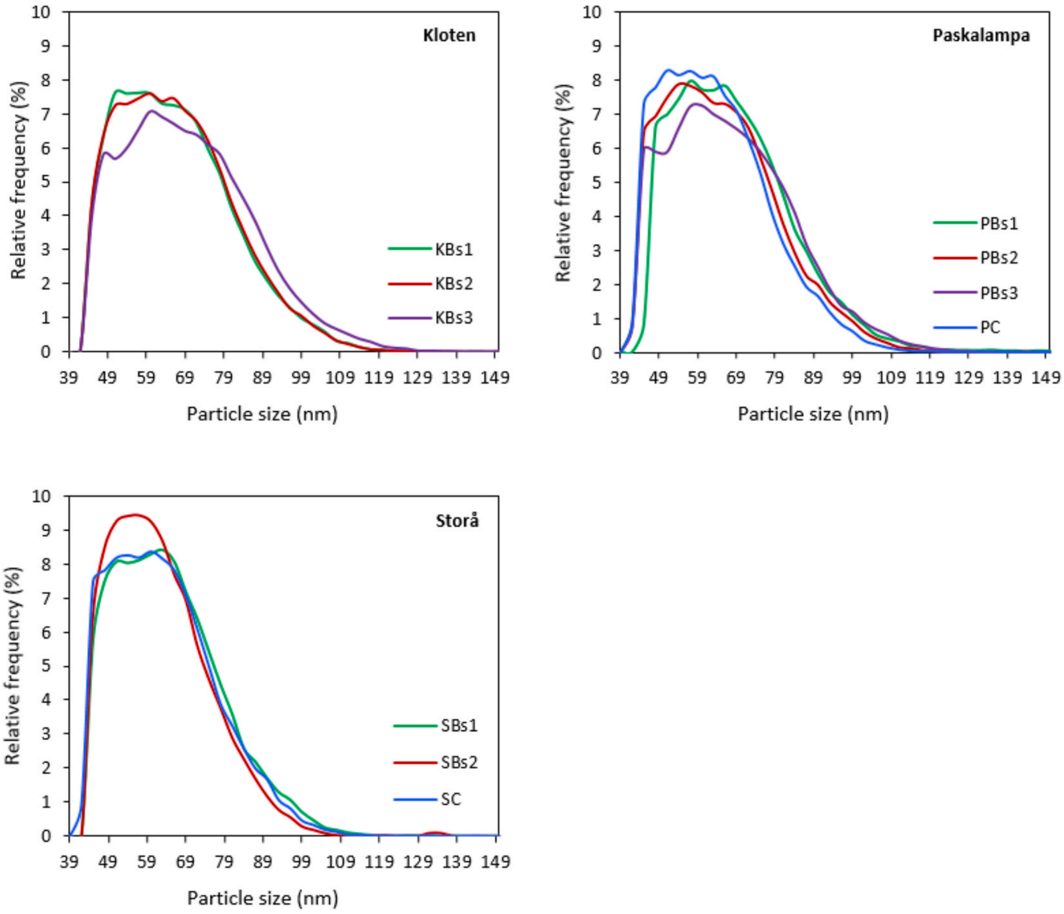

Fig. 5. Particle-size distribution measured by spICP-MS.

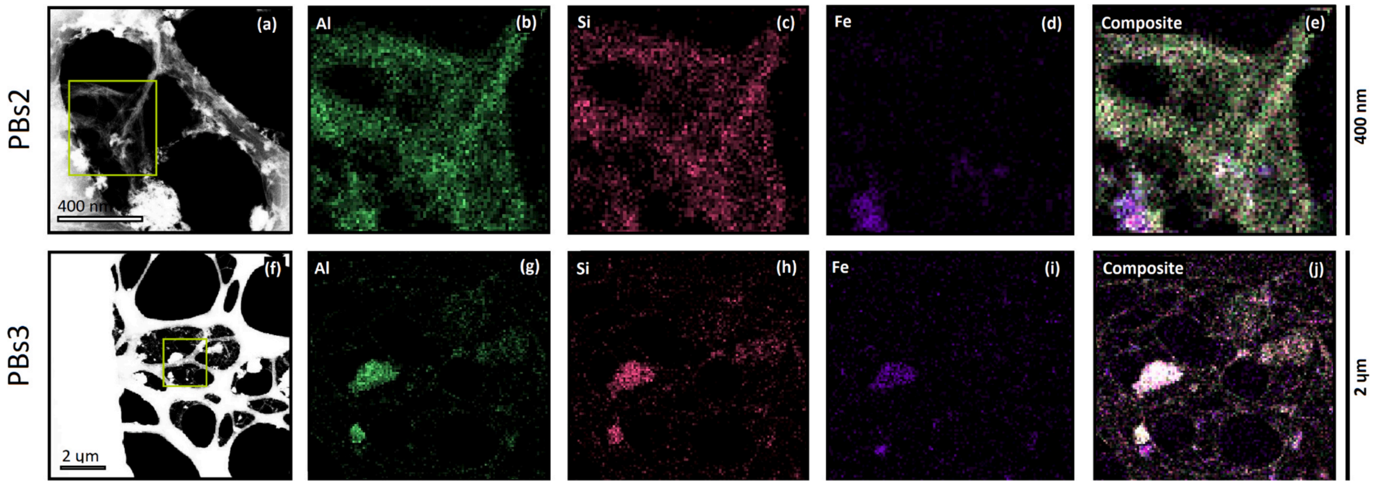

Fig. 6. Elemental maps showing a mix of tubular imogolite and PIM-clusters. Green: Aluminium, red: Silicon, purple: Iron. (For interpretation of the references to colour in this figure legend, the reader is referred to the web version of this article.)

imogolite, often intergrown with them. Picot et al. (2023) studied the growth kinetics of imogolite in synthetic suspensions and found that PIM occurred together with imogolite even after an extended growth stage. They hypothesized that the PIM they found was not able to develop towards a full tubular stage, not even after lengthy polymerisation periods. Further, in dynamic soil systems, PIM will constantly form and dissolve (Kleja et al., 2005). Since PIM is less thermodynamically stable than well-developed imogolite, it is plausible that the former dissolve when in contact with e.g., organic acids of root exudates. In such systems, the life span of part of the PIM may be too short to ever develop into imogolite, leading to the local co-occurrence of newly formed PIM and highly polymerised tubular imogolite.

In all soils, the median ITN particle sizes as determined by spICP-MS were significantly larger than the known size of singular imogolite nanotubes, which is in agreement with the HR-TEM results, which show significant aggregation of PIM into ~ 50 nm clusters. Hence, spICP-MS determined the size of PIM clusters, rather than that of individual PIM units. PIM forms strong aggregates that are difficult to break up once formed, which makes the determination of the size of individual PIM units inside the clusters a difficult task. Moreover, the use of more aggressive dispersion methods would risk damaging the structure.

The common occurrence of PIM in Podzols, together with their high reactivity, stresses the need for detailed characterisation. The traditional view is that PIM occurs as roof tile-like particles that, due to electrostatic effects between negatively charged ≡Si–OH groups and positively charged ≡Al–OH groups, may stack or assemble themselves to form either spherules or tube fragments. Contrary to this, we found three different types of PIM morphologies having varying degree of *para*-crystallinity. Thus, our results show that the traditional view may not be complete and that additional morphologies should be considered. Other studies recently reported similar observations (Adams et al., 2024; Picot et al., 2023).

4.2. *Elemental composition of ITN and the association with Fe*

There were no evidence of Fe atoms being associated with tubular imogolite. Instead, the elemental mapping showed Fe to be concentrated in the PIM particles, particularly to Type 1 PIM clusters. Within such clusters, Al, Si and Fe were evenly distributed, showing no preference for assembling along the particle edges.

ITN are abundant in the spodic B horizon of forest soils and incorporation of Fe(III) in the structure may affect its structural and chemical properties, leading to altered surface charge effects. Fe was found to some extent in all B horizons, but generally in smaller amounts in the ITN-rich samples. Under acidic conditions, Fe(III) is to some extent mobile and may become incorporated into the PIM structure. A plausible consequence of this is an altered affinity towards adsorbing ions, to one that is different to that of PIM and Fh separately.

There is little information in the literature regarding the properties of Fe sorbed on ITN. In an Fe K-edge XAFS study, Baker et al. (2014) concluded that Fe substituted for octahedrally coordinated Al as well as forming surface-sorbed polynuclear complexes on allophane and imogolite. Thus, the Fe in the Type 1 PIM clusters may be substituted into the PIM structure or present as an adsorbed polynuclear Fh-like phase – however, the even distribution within the particles is inconsistent with large Fh clusters.

4.3. *Implications for adsorption modelling*

Since PIM is generally the dominant form of ITN and possesses a greater number of singly coordinated ≡AlOH groups compared to imogolite, the role of imogolite in oxyanion adsorption is likely minimal in comparison to the contribution of PIM and can therefore be considered negligible. Hence, to properly design an adsorption model for ITN, the properties of PIM clusters consisting of agglomerations of discrete PIM units, must be in focus, instead of just the individual particles. Although the nanoparticle size of each individual PIM unit makes lateral interactions between neighbouring ≡AlOH groups comparably small, similar to the case on nanosized Fh (Hiemstra and Zhao, 2016), the overall effect on the surface charge properties appears uncertain, due to the proximity to other PIM units with overlapping electrostatic fields within each cluster. For this reason, the authors hypothesize that the application of Hiemstra and Zhao's size-dependency model for correcting the Stern layer capacitance for flat planes (Hiemstra and Zhao, 2016) is not relevant for soil PIM. In the absence of more precise information on the surface-charge properties, it seems premature to invoke similar corrections for PIM as for Fh.

Moreover, the effect of Fe substitution and adsorption in the PIM clusters will probably need to be considered for accurate assessments of the surface charge properties of both ITN and Fh. The amount and ratio of Fe found in PIM clusters suggest that some of the Fe could be present as an adsorbed polynuclear phase, which may have Fh-like properties. This is likely to affect model parameters such as the acidity constants of the Fh and ITN components in a surface complexation model, although additional research is needed to quantify the associated effects.

5. Conclusion

The current study has characterised the distribution, morphology, and chemical composition of ITN in three Podzols, which has led to the following conclusions:

- ITN occur in unusually high amounts in the lower part of two of the studied B horizons, as evidenced by oxalate-extractable Al and Si. Although the presence of ITN in Podzols has previously been established, their predominant role among secondary Al precipitates has been confirmed.
- PIM dominates the ITN in the studied soils, while tubular imogolite have a lower contribution for ion adsorption reactions present in soils.
- Three types of PIM morphologies were identified from HR-TEM imaging: Type 1 – amorphous structureless cluster, Type 2 – short or fractured nanotubes, and Type 3 – globular aggregates. Among these, the Type 1 cluster was by far the most commonly occurring.
- SpICP-MS analysis showed that PIM predominately forms clusters ~ 50 nm in size.
- In the studied soils, Fe is typically present as a combination of surface-sorbed and substituted phases associated with PIM. However, this phase combination involving Fe has not been observed in association with Imogolite.

CRediT authorship contribution statement

Tove Florén: Writing – original draft, Visualization, Investigation, Formal analysis. **Manuel Bartolomé Díaz:** Writing – review & editing, Investigation. **Geert Cornelis:** Writing – review & editing, Supervision, Methodology. **Stephen Hillier:** Writing – review & editing, Methodology, Investigation. **Jon Petter Gustafsson:** Writing – review & editing, Supervision, Funding acquisition.

Declaration of competing interest

The authors declare that they have no known competing financial interests or personal relationships that could have appeared to influence the work reported in this paper.

Acknowledgements

This study was funded by the Swedish Research Council, project ID no. 2021-04038_VR. Lunjie Zheng at the Material Analysis Laboratory at Chalmers University of Technology, Gothenburg, Sweden, is acknowledged for his work operating the TEM instrument and proving help with interpretation. Gulaim Seisenbaeva at the Department of Molecular Sciences, Swedish University of Agricultural Sciences, Uppsala, Sweden, is acknowledged for collecting FTIR spectra and operating the FTIR spectrometer.

Appendix A. Supplementary data

Supplementary data to this article can be found online at https://doi.org/10.1016/j.geoderma.2025.117376.

Data availability

Data will be made available on request.

References

Adams, F.T., Bauer, M., Levard, C., Michel, F.M., 2024. Multivariate regression analysis of factors regulating the formation of synthetic aluminosilicate nanoparticles. Nanoscale 16, 6561–6572. https://doi.org/10.1039/D4NR00473F.

Arai, Y., Sparks, D.L., Davis, J.A., 2005. Arsenate adsorption mechanisms at the allophane−water Interface. Environ. Sci. Tech. 39, 2537–2544. https://doi.org/10.1021/es0486770.

Arancibia-Miranda, N., Escudey, M., Molina, M., García-González, M.T., 2011. Use of isoelectric point and pH to evaluate the synthesis of a nanotubular aluminosilicate. J. Non-Cryst. Solids 357, 1750–1756. https://doi.org/10.1016/j.jnoncrysol.2011.01.012.

Arancibia-Miranda, N., Manquián-Cerda, K., Pizarro, C., Maldonado, T., Suazo-Hernández, J., Escudey, M., Bolan, N., Sarkar, B., 2020. Mechanistic insights into simultaneous removal of copper, cadmium and arsenic from water by iron oxide-functionalized magnetic imogolite nanocomposites. J. Hazard. Mater. 398, 122940. https://doi.org/10.1016/j.jhazmat.2020.122940.

Baker, L.L., Nickerson, R.D., Strawn, D.G., 2014. XAFS Study of Fe-substituted Allophane and Imogolite. Clays Clay Miner. 62, 20–34. https://doi.org/10.1346/CCMN.2014.0620103.

Bazilevskaya, E., Archibald, D.D., Aryanpour, M., Kubicki, J.D., Martínez, C.E., 2011. Aluminum coprecipitates with Fe (hydr)oxides: Does isomorphous substitution of Al3+ for Fe3+ in goethite occur? Geochim. Cosmochim. Acta 75, 4667–4683. https://doi.org/10.1016/j.gca.2011.05.041.

Butler, B.M., Hillier, S., 2021a. powdR: An R package for quantitative mineralogy using full pattern summation of X-ray powder diffraction data. Comput. Geosci. 147, 104662. https://doi.org/10.1016/j.cageo.2020.104662.

Butler, B.M., Hillier, S., 2021b. Automated full-pattern summation of X-ray powder diffraction data for high-throughput quantification of clay-bearing mixtures. Clay Clay Miner. 69, 38–51. https://doi.org/10.1007/s42860-020-00105-6.

Chen, W., Wee, P., Brindle, I.D., 2000. Elimination of the memory effects of gold, mercury and silver in inductively coupled plasma atomic emission spectroscopy. J. Anal. At. Spectrom 15, 409–413. https://doi.org/10.1039/a908658g.

Cornelis, G., Hassellöv, M., 2014. A signal deconvolution method to discriminate smaller nanoparticles in single particle ICP-MS. J. Anal. At. Spectrom 29, 134–144. https://doi.org/10.1039/C3JA50160D.

Cradwick, P.D.G., Farmer, V.C., Russell, J.D., Masson, C.R., Wada, K., Yoshinaga, N., 1972. Imogolite, a hydrated aluminium silicate of tubular structure. Nat. Phys. Sci. 240, 187–189. https://doi.org/10.1038/physci240187a0.

Farmer, V.C., Russell, J.D., Berrow, M.L., 1980. Imogolite and proto-imogolite allophane in spodic horizons: evidence for a mobile aluminium silicate complex in Podzol formation. J. Soil Sci. 31, 673–684. https://doi.org/10.1111/j.1365-2389.1980.tb02113.x.

Gustafsson, J.P., 2001. The surface chemistry of imogolite. Clay Miner. 49, 73–80. https://doi.org/10.1346/CCMN.2001.0490106.

Gustafsson, J.P., 2006. Arsenate adsorption to soils: modelling the competition from humic substances. Geoderma 136, 320–330. https://doi.org/10.1016/j.geoderma.2006.03.046.

Gustafsson, J.P., Bhattacharya, P., Bain, D.C., Fraser, A.R., McHardy, W.J., 1995. Podzolisation mechanisms and the synthesis of imogolite in northern Scandinavia. Geoderma 66, 167–184. https://doi.org/10.1016/0016-7061(95)00005-9.

Gustafsson, J.P., Bhattacharya, P., Karltun, E., 1999. Mineralogy of poorly crystalline aluminium phases in the B horizon of Podzols in southern Sweden. J. Appl. Geochem. 14, 707–718. https://doi.org/10.1016/S0883-2927(99)00002-5.

Gustafsson, J.P., Tiberg, C., 2015. Molybdenum binding to soil constituents in acid soils: An XAS and modelling study. Chem. Geol. 417, 279–288. https://doi.org/10.1016/j.chemgeo.2015.10.016.

Hiemstra, T., Zhao, W., 2016. Reactivity of ferrihydrite and ferritin in relation to surface structure, size, and nanoparticle formation studied for phosphate and arsenate. Environ. Sci. Nano 3, 1265–1279. https://doi.org/10.1039/C6EN00061D.

Hillier, S., 1999. Use of an air brush to spray dry samples for X-ray powder diffraction. Clay Miner. 34, 127–135. https://doi.org/10.1180/000985599545984.

IUSS Working Group WRB, 2022. World Reference Base for Soil Resources. International soil classification system for naming soils and creating legends for soil maps, 4th edition. International Union of Soil Sciences (IUSS), Vienna, Austria.

Jackson, M.L., 1969. Soil Chemical Analysis-advanced Course. Department of Soils. University of Wisconsin, pp. 20–65.

Johnston, C.P., Chrysochoou, M., 2016. Mechanisms of chromate, selenate, and sulfate adsorption on Al-substituted ferrihydrite: implications for ferrihydrite surface structure and reactivity. Environ. Sci. Tech. 50, 3589–3596. https://doi.org/10.1021/acs.est.5b05529.

Karltun, E., Bain, D.C., Gustafsson, J.P., Mannerkoski, H., Murad, E., Wagner, U., Fraser, A.R., McHardy, W.J., Starr, M., 2000. Surface reactivity of poorly-ordered minerals in podzol B horizons. Geoderma 94, 265–288. https://doi.org/10.1016/S0016-7061(98)00141-4.

Kleja, D.B., Standring, W., Oughton, D.H., Gustafsson, J.P., Fifield, K., Fraser, A.R., 2005. Assessment of isotopically exchangeable Al in soil materials using ^{26}Al tracer. Geochim. Cosmochim. Acta 69, 5263–5277. https://doi.org/10.1016/j.gca.2005.06.010.

Lenhardt, K.R., Breitzke, H., Buntkowsky, G., Reimhult, E., Willinger, M., Rennert, T., 2021. Synthesis of short-range aluminosilicates at ambient conditions. Sci. Rep. 11, 4207. https://doi.org/10.1038/s41598-021-83643-w.

Lenhardt, K.R., Breitzke, H., Buntkowsky, G., Mikutta, C., Rennert, T., 2022. Interactions of dissolved organic matter with short-range ordered aluminosilicates by adsorption and co-precipitation. Geoderma 423, 115960. https://doi.org/10.1016/j.geoderma.2022.115960.

Levard, C., Doelsch, E., Basile-Doelsch, I., Abidin, Z., Miche, H., Masion, A., Rose, J., Borschneck, D., Bottero, J.-Y., 2012. Structure and distribution of allophanes, imogolite and proto-imogolite in volcanic soils. Geoderma 183–184, 100–108. https://doi.org/10.1016/j.geoderma.2012.03.015.

Lundström, U.S., Van Breemen, N., Bain, D.C., van Hees, P.A.W., Giesler, R., Gustafsson, J.P., Ilvesniemi, H., Karltun, E., Melkerud, P.-A., Olsson, M., Riise, G., Wahlberg, O., Bergelin, A., Bishop, K., Finlay, R., Jongmans, A.G., Magnusson, T., Mannerkoski, H., Nordgren, A., Nyberg, L., Starr, M., Strand, L.T., 2000. Advances in understanding the podzolization process resulting from a multidisciplinary study of three coniferous forest soils in the Nordic Countries. Geoderma 94, 335–353. https://doi.org/10.1016/S0016-7061(99)00077-4.

McKeague, J.A., 1967. An evaluation of 0.1 M pyrophosphate and pyrophosphate-dithionite in comparison with oxalate as extractants of the accumulation products in podzols and some other soils. Can. J. Soil Sci. 47, 95–99. https://doi.org/10.4141/cjss67-017.

Mossin, L., Mortensen, M., Nørnberg, P., 2002. Imogolite related to podzolization processes in Danish Podzols. Geoderma 109, 103–116. https://doi.org/10.1016/S0016-7061(02)00145-3.

Pace, H.E., Rogers, N.J., Jarolimek, C., Coleman, V.A., Higgins, C.P., Ranville, J.F., 2011. Determining transport efficiency for the purpose of counting and sizing nanoparticles via single particle inductively coupled plasma mass spectrometry. Anal. Chem. 83, 9361–9369. https://doi.org/10.1021/ac201952t.

Parfitt, R.L., 2009. Allophane and imogolite: role in soil biogeochemical processes. Clay Miner. 44, 135–155. https://doi.org/10.1180/claymin.2009.044.1.135.

Parfitt, R.L., 1989. Phosphate reactions with natural allophane, ferrihydrite and goethite. J. Soil Sci. 40, 359–369. https://doi.org/10.1111/j.1365-2389.1989.tb01280.x.

Parfitt, R.L., Hemni, T., 1980. Structure of some allophanes from New Zealand. Clays Clay Miner. 28, 285–294. https://doi.org/10.1346/CCMN.1980.0280407.

Picot, P., Lange, T., Testard, F., Gobeaux, F., Thill, A., 2023. Evidence and importance of intermediate nanostructures in the journey from molecular precursors to allophane and imogolite nanocrystals. App. Clay Sci. 241, 107013. https://doi.org/10.1016/j.clay.2023.107013.

Rasband, W.S., ImageJ, U. S. National Institutes of Health, Bethesda, Maryland, USA, https://imagej.net/ij/, 1997-2018.

Shafia, E., Esposito, S., Manzoli, M., Chiesa, M., Tiberto, P., Barrera, G., Menard, G., Allia, P., Freyria, F.S., Garrone, E., Bonelli, B., 2015. Al/Fe isomorphic substitution versus Fe2O3 clusters formation in Fe-doped aluminosilicate nanotubes (imogolite). J. Nanopart. Res. 17, 336. https://doi.org/10.1007/s11051-015-3130-2.

Shafia, E., Esposito, S., Armandi, M., Manzoli, M., Garrone, E., Bonelli, B., 2016. Isomorphic substitution of aluminium by iron into single-walled alumino-silicate nanotubes: A physico-chemical insight into the structural and adsorption properties of Fe-doped imogolite. Microporous Mesoporous Mater. 224, 229–238. https://doi.org/10.1016/j.micromeso.2015.11.044.

Soil Survey Staff. 2022. Keys to Soil Taxonomy, 13th edition. USDA Natural Resources Conservation Service.

Hiemstra, T., Yong, H., van Riemsdijk, W.H., 1999. Interfacial charging phenomena of aluminum (hydr)oxides. Langmuir 15, 5942–5955. https://doi.org/10.1021/la981301d.

Tiberg, C., Sjöstedt, C., Eriksson, A.K., Klysubun, W., Gustafsson, J.P., 2020. Phosphate competition with arsenate on poorly crystalline iron and aluminum (hydr)oxide mixtures. Chemosphere 255, 126937. https://doi.org/10.1016/j.chemosphere.2020.126937.

Tiberg, C., Sjöstedt, C., Gustafsson, J.P., 2018. Metal sorption to Spodosol Bs horizons: Organic matter complexes predominate. Chemosphere 196, 556–565. https://doi.org/10.1016/j.chemosphere.2018.01.004.

Tuyishime, J.R.M., Adediran, G.A., Olsson, B.A., Spohn, M., Hillier, S., Klysubun, W., Gustafsson, J.P., 2022. Phosphorus abundance and speciation in acid forest Podzols – Effect of postglacial weathering. Geoderma 406, 115500. https://doi.org/10.1016/j.geoderma.2021.115500.

van Reeuwijk, L.P., 2002. Procedures for Soil Analysis, 6th ed. International Soil Reference and Information Centre, Wageningen, Netherlands.

Wada, K., Yoshinaga, N., 1969. The structure of imogolite. Am. Mineral. 54, 50–71.

Wang, Y., Saito, T., Fakhreddine, S., Nagasaki, S., 2023. Mechanisms of selenate adsorption at the imogolite-water interface. Colloids Surf., A Physicochem. Eng. Asp. 656, 130444. https://doi.org/10.1016/j.colsurfa.2022.130444.